An adhesive DPD wall model for dynamic wetting

B. Henrich[1,2], C. Cupelli[3], M. Moseler[2,1] and M. Santer[2,3]

[1] *FMF-Freiburg Materials Research Center, University of Freiburg - Stefan-Meier-Straße 21,*
D-79104 Freiburg, Germany
[2] *IWM-Fraunhofer Institute for the Mechanics of Materials - Wöhlerstraße 11, D-79108 Freiburg, Germany*
[3] *IMTEK-Institute for Microsystem Technology, Laboratory for MEMS applications - Georges-Köhler-Allee 106,*
D-79110 Freiburg, Germany

Abstract – A novel method for the treatment of solid-liquid interfaces in the framework of dissipative particle dynamics (DPD) is presented. The solid is represented by an amorphous, thermally rough ensemble of particles. Since the density of this phase is chosen commensurate to the liquid, artefacts of alternative wall models such as particle layering or spurious variations in temperature are avoided. An adjustable static contact angle permits the convenient study of complex wetting phenomena. We explore the physical behaviour of this boundary model with respect to bulk Poiseuille and Couette flow as well as forced wetting and the behaviour of dynamic contact angles.

Introduction. – Phenomena involving dynamic spreading of fluids on solid surfaces are of great importance in many traditional industrial processes, but also in modern micro- and nanofluidics applications like passive transport, structuring and supply of small amounts of liquids [1]. The general dynamics of capillary-driven flow in arbitrary geometries is cumbersome to study with conventional mesh-based computational fluid dynamics (CFD) methods that solve the discretized Navier-Stokes equations (NSE). Difficulties not only arise in representing the shape and dynamics of a capillary meniscus [2], but also in resolving the microscopic region where it contacts the boundary [3].

Kinetic simulation schemes such as the grid-based Lattice Boltzmann method (see [4] and references therein) or meshless, particle-based methods such as dissipative particle dynamics (DPD) [5–7] permit to address these problems in novel ways [8]. Originally invented to model the dynamics of solvents on mesoscopic length and time scales, hydrodynamics is represented by the collision dynamics of an ensemble of pseudo-atoms. Fluid properties but also flow boundary conditions emerge as a consequence of the chosen particle interactions.

In this respect, especially DPD is receiving a rapidly increasing number of contributions as it bears some resemblance with molecular dynamics: the particle dynamics is governed by Newton's equation of motion and a generic equation of state can be adopted by including appropriate conservative inter-particle forces. Within the so-called many-body DPD (MDPD), liquid-vapor (*lv*-) coexistence can be achieved by making the forces density dependent [9] or deriving them from an appropriate excess free energy [10]. With a suitable choice of model parameters, the vapour phase can be suppressed in favour of a sharp *lv*-interface [9,11] that can easily be tracked and visualized. At least for scales larger than the thermal capillary length, below which thermal fluctuations dominate, the statics [9] as well as the dynamics [12] of capillary *lv*-interfaces compare well to continuum solutions.

In modeling solid-liquid (*sl*-) interfaces most emphasis has been put on imposing rigorous macroscopic boundary conditions (BC), such as *no slip* at sharply defined impenetrable interfaces. This originates from a strictly mesoscopic interpretation of DPD, where single particles represent "lumps of fluid" on scales well above atomistic ones [7]. In general then, the forces exerted on the liquid at the interface must be matched carefully in order to avoid spurious behaviour such as particle layering [13], variations in temperature [14] or artificial slip [15]. This has led to rather specialized constructions involving mostly flat [13,15] or spherically curved *sl*-interfaces [16,17]. In some cases it has been found

useful to represent the solid by yet another liquid phase without an actual solid structure [11,17].

For studying wetting phenomena on structured or patterned substrates [18], available rigorous boundary models appear rather difficult to handle. In this work we introduce a solid boundary model that circumvents the above-mentioned problems in a much simpler way, by representing the solid by an amorphous, thermally rough configuration of particles, resulting in a thin diffuse *sl*-interface. We show how together with an MDPD scheme a flexible framework for representing dynamic wetting on possibly textured boundaries emerges.

This paper is organized as follows: after briefly outlining the MDPD scheme, we illustrate the construction of the boundary model, which is in turn investigated phenomenologically with respect to wetting behaviour, flow boundary conditions, and forced wetting including the characteristics of dynamic contact angles.

The many-body DPD scheme. – In DPD, particles interact via pairwise central forces $\mathbf{F}_{ij} = \mathbf{F}_{ij}^{\mathrm{R}} + \mathbf{F}_{ij}^{\mathrm{D}} + \mathbf{F}_{ij}^{\mathrm{C}}$. If $\mathbf{r}_i$ denotes the particle position and $\mathbf{v}_i$ its velocity, the conservative force in standard DPD is $\mathbf{F}_{ij}^{\mathrm{C}} = A w^{\mathrm{C}}(r_{ij}) \mathbf{e}_{ij}$, where $\mathbf{r}_{ij} = \mathbf{r}_i - \mathbf{r}_j$, $r_{ij} = |\mathbf{r}_{ij}|$ and $\mathbf{e}_{ij} = \mathbf{r}_{ij}/r_{ij}$. The weight function $w^{\mathrm{C}}(r)$ vanishes for an inter-particle distance r larger than a cutoff radius r_{c}.

The random and dissipative forces are $\mathbf{F}_{ij}^{\mathrm{R}} = q w^{\mathrm{R}}(r_{ij}) \times \xi_{ij} \mathbf{r}_{ij}$ and $\mathbf{F}_{ij}^{\mathrm{D}} = -\gamma w^{\mathrm{D}}(r_{ij})(\mathbf{v}_{ij} \cdot \mathbf{e}_{ij}) \mathbf{e}_{ij}$, respectively, where $\mathbf{v}_{ij} = \mathbf{v}_i - \mathbf{v}_j$. These forces constitute a thermostat if the amplitudes q of the random variable ξ_{ij} and the viscous dissipation γ satisfy a fluctuation-dissipation theorem: $q^2 = 2\gamma k_{\mathrm{B}}T$ and $w^{\mathrm{R}}(r)^2 = w^{\mathrm{D}}(r)$, where $k_{\mathrm{B}}T$ denotes the desired temperature in units of Boltzmann's constant k_{B}. To integrate the resulting equations of motion, we use a velocity Verlet algorithm [19] with a particle mass $m = 1$ and a time step $dt = 0.01$.

The conservative interaction $\mathbf{F}^{\mathrm{C}}$ is usually derived from a rather soft and unspecific weight function w^{C}, permitting a fairly large integration time step. A common choice for w^{C} which we also use in this paper is $w^{\mathrm{C}} = (1 - r/r_{\mathrm{c}})$ and $w^{\mathrm{R}} = w^{\mathrm{C}}$. It follows that the EOS becomes at most quadratic in the average particle density ρ.

Liquid-vapor interfaces and hence free capillary surfaces can only exist for more complex EOS, and $\mathbf{F}_{ij}^{\mathrm{C}}$ must then be augmented by density-dependent contributions [9,10,20]. This class of schemes is termed multi-body DPD (MDPD). Here, the approach of Warren [9] is pursued in which the repulsive part of the force depends on a weighted average of the particle density, while the attractive part is density independent:

$$\mathbf{F}_{ij}^{\mathrm{C}} = A_{ij} w^{\mathrm{C}}(r_{ij}) \mathbf{e}_{ij} + B(\bar{\rho}_i + \bar{\rho}_j) w_{\mathrm{d}}(r_{ij}) \mathbf{e}_{ij}, \qquad (1)$$

with an additional weight function $w_{\mathrm{d}}(r) = 15/(2\pi r_{\mathrm{d}}^3) \times (1 - r/r_{\mathrm{d}})^2$. In eq. (1) we let A_{ij} depend on a pair of particle indices, allowing us to distinguish between interactions within the liquid (l) ($A_{ll} \equiv A = -40.0$), the solid (s) ($A_{ss} \equiv A$) and across the solid-liquid (sl)-interface (A_{sl}).

Table 1: The simulation parameters vary only slightly from the ones used in [9] ($A = -40.0$, $B = 25.0$, $\rho = 6.08$). All quantities are given in model units (m.u.). All simulation results are at $r_{\mathrm{c}} = k_{\mathrm{B}}T = 1$.

Parameter	Symbol	m.u.
Fluid particle density	ρ	6.00
Interaction range (attr.)	r_{c}	1.0
Interaction range (rep.)	r_{d}	0.75
Amplitude of $\mathbf{F}^{\mathrm{R}}$	q	6.00
Attraction parameter	A	-40.0
Repulsion parameter	B	25.0
Surface tension	σ	7.51 ± 0.04
Viscosity	η	7.41 ± 0.06

We will show that A_{sl} can be used to adjust the static wetting behaviour. The repulsive part with $B > 0$ acts over a slightly smaller interaction radius r_{d}. $\bar{\rho}_i$ at the location of particle i is the instantaneously weighted average density $\bar{\rho}_i = \sum_{i \neq j} w_{\mathrm{d}}(r_{ij})$. All simulation parameters are given in table 1. Throughout this paper all quantities are given in model units.

The boundary model. – Equation (1) implies that the force law depends on the local environment. With respect to a mesoscopic point of view, this environment should be the same also for particles directly at the *sl*-interface. We illustrate how this can be achieved by creating a *sl*-system consisting of a liquid film confined between two walls. Starting with a free-standing equilibrated, planar slab of fluid of thickness $24r_{\mathrm{c}}$ in the *x*-direction and dividing it into two boundary regions of thickness $2r_{\mathrm{c}}$ and an inner (liquid) region of thickness $20r_{\mathrm{c}}$, the nominal positions $x_{\mathrm{int}} = \pm 10r_{\mathrm{c}}$ of the *sl*-interfaces are defined. Periodic boundary conditions are applied in the *y*- and *z*-direction with a periodicity of $12r_{\mathrm{c}} \times 20r_{\mathrm{c}}$.

At some time t_0 after equilibration (already 300 integration time steps suffice), each particle i at position $\mathbf{r}_i(t_0) = (x_i(t_0), \ y_i(t_0), \ z_i(t_0))$ with $|x_i(t_0)| > |x_{\mathrm{int}}|$ is permanently attached to the site $\mathbf{r}_i(t_0)$ by a spring force $\mathbf{F}_w = -k_{\mathrm{s}}(\mathbf{r}_i(t) - \mathbf{r}_i(t_0))$, leading to solidification of the boundary regions. To be consistent with eq. (1), the inter-particle interactions in the solid are kept, only the value of A_{sl} is then set according to the desired wetting conditions. Additionally, a weak external repelling force $\mathbf{F}_{\mathrm{ext}}$ acting on liquid particles beyond x_{int}, *i.e.* within the solid boundary, is employed to keep isolated liquid particles from diffusing into the solid phase indefinitely, see upper panel of fig. 1.

After a short re-equilibration, a sharp but smooth interface develops, shown for $A_{sl} = -35.0$ and $k_{\mathrm{s}} = 3.0$, in fig. 1a) (thick solid line), where the interface width is less than $1r_{\mathrm{c}}$. The liquid density profile induced by this amorphous, thermally roughened wall is compared with two other realisations of a solid phase: i) a frozen amorphous
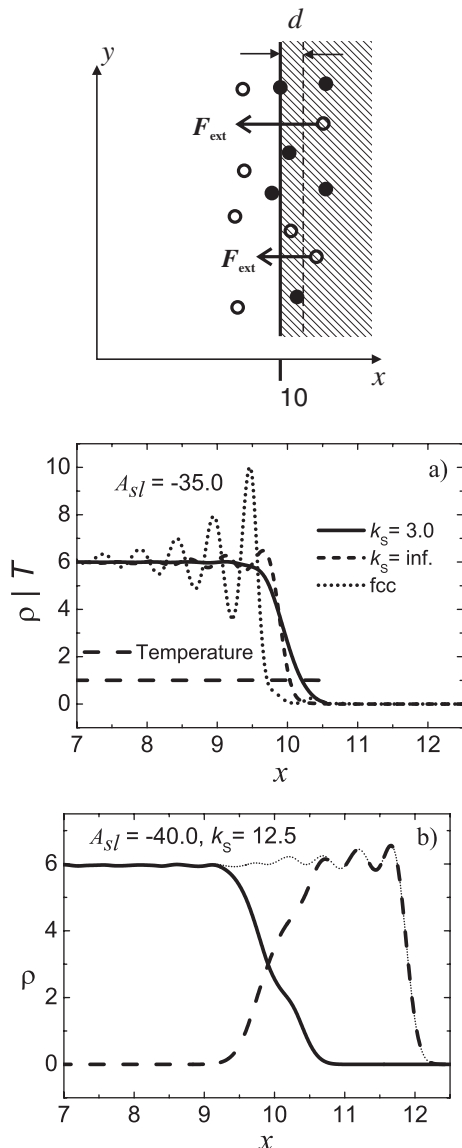
Fig. 1: Density profiles depending on the slit coordinate x. Upper panel: schematic of the diffuse interface (full dots: solid phase, circles: liquid). For $|x| > |x_{int} \pm d|$, $d = 0.25r_c$, $\mathbf{F}_{ext} = -B(x - (x_{int} \pm d))$ acts on liquid particles only to prevent indefinite diffusion into the wall. a) Density distributions of the liquid for a partially wetting wall and varying k_s. The temperature T is measured for $k_s = 3.0$. b) Density profile in the case of complete wetting, $A_{sl} = -40.00$ and $k_s = 12.5$. Thick solid line: particle density distribution of the liquid phase. Thick dashed line: density distribution within the solid phase. Dotted line: sum of both densities. In both cases, a) and b), the sl-interface is located at $x_{int} = 10.0$.

structure resulting from particle positions at t_0 ($k_s = \infty$), and ii) a frozen, crystalline fcc (100)-surface of the same density. In both cases the solid phase induces pronounced density oscillations in the liquid. These seem already significantly reduced in case i), but this mainly originates from spatial averaging in the y- and z-direction. Thermal roughening also results in a smooth density profile locally

due to dynamical averaging. The spring constant k_s was chosen as to render the net density profile flat, and to make the width of the interfacial region as small as possible. For partial wetting, k_s can be given a relatively low value, as the sl-interface already stabilizes due to a reduced attraction between the particle species ($A_{sl} > -40$). Approaching complete wetting k_s must be increased accordingly, in order to stabilize the interface. Figure 1b) shows the density profile for $A_{sl} = -40$, where $k_s = 12.5$ was found to yield a satisfactory profile stable at a width of $\simeq 1.5r_c$. We note that the role of the soft external potential $\mathbf{F}_{ext}$ can also be replaced by a sufficiently dense layer of "ghost" particles that interact only with particles of the liquid. Together with this extra layer, the shape of the initially chosen dividing line between liquid and solid phase (here the plane at x_{int}) may then be chosen to realize more complicated surface geometries such as cavities.

Strictly speaking, a definite location of the sl-interface (e.g. the initially chosen x_{int}) is not unambiguously defined any more (though the density profiles of the solid and the liquid are rather symmetric at x_{int} in all cases). Under flow conditions, the slight inter-penetration of the solid and the liquid phase (cf. fig. 1b)) will make the mass flow $j_z(x) = v_z(x)\rho(x)$ vary smoothly across the interface (depending on its thickness and also on the wetting conditions). However, one may now identify *effective* interface positions (denoted as $\overline{x}_{int}$) not as a free parameter, but as the physically most appropriate choice that in the following will be inferred from the simulation data of Poiseuille- and Couette flow. In fig. 2a), the profiles $j_z(x)$ of body-force driven slit flow are displayed, generated with a constant body force $F_g = 0.02$, for $A_{sl} = -40.0$ and -35.0. In both cases the current density profile $j_z(x)$ can well be fitted to a Poisseuille parabola in the range $|x| < 9.5r_c$, i.e. $j_z(x) \simeq -1/2x^2\rho^2 F_g/\eta + j_{max}$, where the viscosity $\eta = 7.41 \pm 0.06$ was determined in an independent simulation following [21]. Only small deviations occur in the interface region, see inset in fig. 2a). A detailed view of $j_z(x)$ at the nominal interface $x_{int} = 10r_c$ shows that a slightly negative slip is present for $A_{sl} = -40.0$. For $A_{sl} = -35.0$, we observe a positive slip. In the latter case (partial wetting) the sl-interface is relatively sharp (cf. fig. 1a)), and one may set $\overline{x}_{int} \simeq x_{int}$, if a well-defined positive slip length L_s with respect to x_{int} exists. At complete wetting, the interface and thus the diffusive width of the solid phase becomes broader and effectively forces j_z to zero before reaching x_{int}. This can be considered as a displacement of the effective interface position inwards if it is, e.g., independent of the shear rate. The displacement then equals a well-defined negative slip length, and we have $\overline{x}_{int} = x_{int} + L_s$ in this case, where L_s is a fraction of r_c. This interpretation is in fact sustained by considering A_{sl}-dependent slip lengths L_s determined from Couette flow simulations (fig. 2b)). With sheared boundaries moving at constant wall velocities $\pm v_{wall}$, we define L_s by $\overline{v}_z(x_{int}) - v_{wall} = L_s \partial \overline{v}_z(x)/\partial x$, $x = x_{int}$, where $\overline{v}_z(x_{int})$ is the extrapolation of the flow field $v_z(x)$ at x_{int}. From
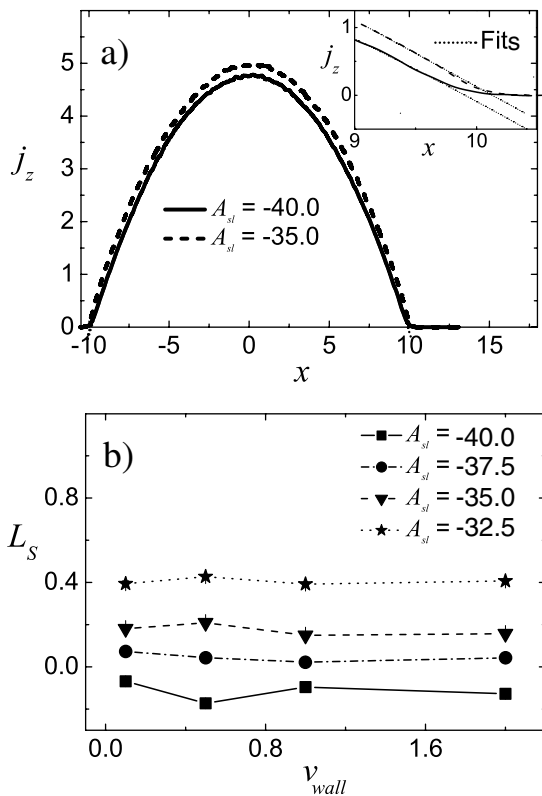
Fig. 2: Behavior of boundary conditions. a) Profiles of current densities for different wetting conditions. The inset shows a magnification of the current density profile in the vicinity of the interface; by extrapolating the fit to a parabola towards x_{int}, an effective slip velocity can be inferred (exemplified by the thin dotted lines). b) Wetting-dependent slip lengths L_{s} as functions of v_{wall}. Error bars are of the order of symbol thickness.

fig. 2b) one infers that except close to complete wetting $L_{\text{s}} > 0$. The constancy of L_{s} with respect to v_{wall} (*i.e.* the shear rate) indicates that the *sl*-interface leads to a Navier-type slip mechanism. L_{s} increases with A_{sl}, *i.e.*, with increasing hydrophobicity of the solid. This tendency is also found in MD simulations with Lennard-Jones potentials [22]. We find that $\overline{x}_{\text{int}}$ as defined above is fully consistent with all contact angle measurements in the following.

Along with the Couette flow simulations, we also verified that the profiles of each temperature component (*e.g.* $k_{\text{B}}T_x = \langle v_x^2 \rangle$) across the interface is constant, which is to be expected by the nature of the interface.

The static contact angle θ_0 can actually be set in a simple way by varying A_{sl}. The range of θ_0 goes from $\simeq 0°$ to almost $180°$, see fig. 3b). θ_0 as a function of A_{sl} can be inferred from Young's equation, $\gamma_{sv} - \gamma_{sl} = \gamma_{lv}\cos(\theta_0)$, using the interfacial and surface tensions between the phases, γ_{sl}, γ_{sv} and γ_{lv}. These have been determined by a standard procedure for hetero-interfaces [18]. For instance, γ_{sl} is obtained from $\gamma_{sl} = \int [p_{xx} - 1/2(p_{yy} + p_{zz}) - \phi]\, dx$, where p_{ij} $(i, j = x, y, z)$ denote the components of the
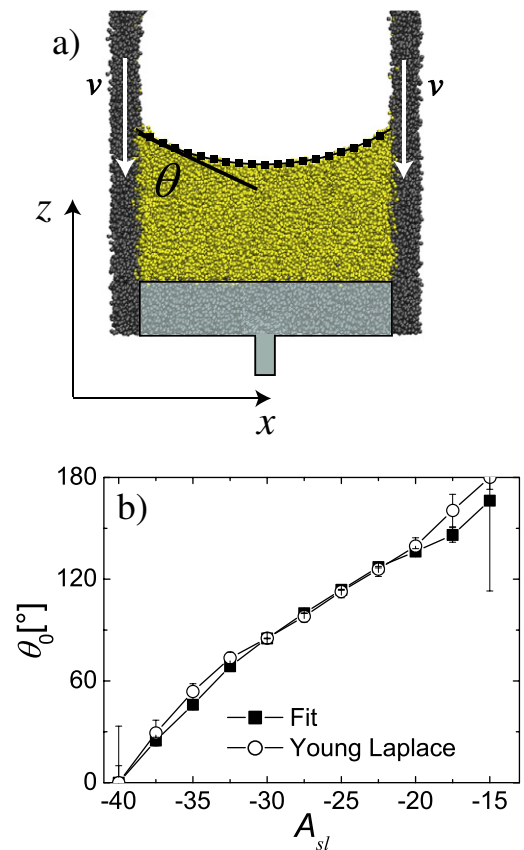
Fig. 3: Wetting behaviour. a) Setup for measuring static $(\theta = \theta_0)$ and dynamic contact angles $(\theta = \theta_{\text{d}})$ as described in the text. The values of the mass histogram (measured from the upper piston level) are shown as black squares. The histogram is fitted to a circle segment (black solid line), θ is measured with respect to the plane at $\overline{x}_{\text{int}}$. b) The static contact angle as a function of A_{sl}. The error bars at the extreme values $(\theta_0 = 0°$ and $\theta_0 = 180°)$ denote the maximum error resulting from a diverging derivative in the error calculation. In the range from $A_{sl} = -37.5$ to $A_{sl} = -20.0$ the error bars are in the order of the symbol thickness.

pressure tensor with respect to the forces in eq. (1), the integration is over a control volume containing the interface. The pinning forces do not cause residual stress as the particle configuration of the solid phase has been relaxed beforehand. ϕ comprises all external forces acting on the liquid [23], *i.e.* $\mathbf{F}_{\text{ext}}$ in our case. By construction, its contribution should be small, and is indeed found to be $< 5\%$ in all cases. For the *lv*-interface, we have $\phi = 0$ and a value of $\gamma_{lv} = \sigma = 7.51 \pm 0.04$ for the surface tension is recovered, in accord with [9].

The definition employing interfacial tensions is fully consistent with a geometrical procedure to measure θ_0 (see fig. 3a)): a liquid plug is placed in a slit, confined in the x-direction and supported by an adhesive piston in the z-direction, with periodic BC in the y-direction. The fluid plug develops a symmetric meniscus whose shape has been extracted by histogramming the amount of fluid
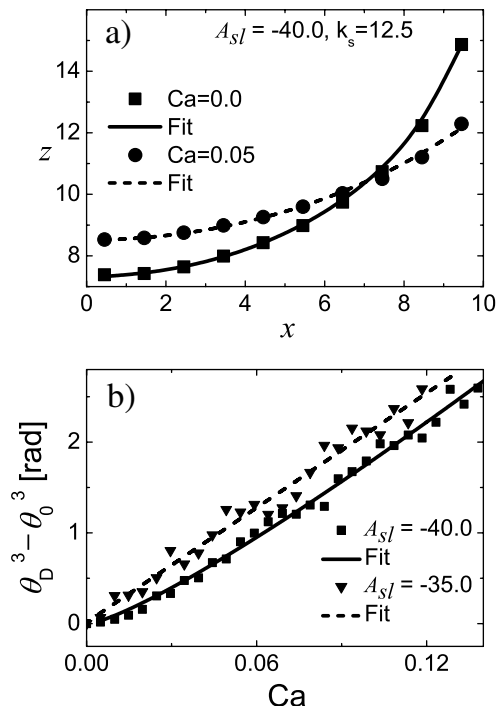
Fig. 4: Contact angles. a) Meniscus profiles in the case of complete wetting ($A_{sl} = -40.0$) for $Ca = 0.0$ and 0.05. The z-axis denotes the vertical position in the slit, the piston is at $z = 0$. b) θ_0 as a function of Ca. Data sets are fitted with the model of Cox [24] ($A_{sl} = -35.0$) and Eggers [25], respectively (see text). Error bars are of the order of the symbol thickness.

contained in equally spaced slices in the x-direction. This histogram is then fitted to a circle segment, and θ_0 is taken as the angle of inclination of the segment with the plane at $\overline{x}_{int}$. Figure 2b) shows that within numerical errors both methods to determine $\theta_0(A_{sl})$ agree.

In a similar manner we can also infer a dynamic contact angle θ_d emerging under forced wetting, which can be emulated by moving the walls in fig. 3a) downwards at a velocity v while keeping the piston fixed. In fig. 4a), the meniscus shape evolving at $v \simeq 0.05$ is compared to the corresponding one at rest. The significance of θ_d is that in a dynamical situation θ_d sets the actual driving capillary pressure and thus influences fluid motion globally. More generally, one considers θ_d as a function of the capillary number $Ca = \eta v / \sigma$, which measures the opposing influences of viscous and capillary forces.

We note that in an analytical continuum treatment of dynamic wetting, a relation $\theta_d(Ca)$ cannot be inferred from a straightforward solution of the NSE assuming stick boundary conditions, which would lead to a singularity of the viscous stresses at the contact line (CL) [26]. To describe CL motion consistently, additional models for the microscopic region where the meniscus meets the solid boundary must be employed, leading to effective continuum models [3,25]. One should stress that, despite the coarse-grained character of the DPD

approach, such supplementary models are not required here as a prerequisite. Any phenomenon of liquid flow is ultimately determined by the fundamental particle interactions and kinetics, *i.e.*, a particular relation $\theta_0(Ca)$ is already implied with the model one provides for the *sl*-interface. Artefacts such as the above-mentioned stress singularity naturally do not arise. This is quite analogous to atomistic modelling of *sl*-systems with MD. There, it is often found that the generic behaviour of CL dynamics can actually be understood in terms of an effective continuum model, even for small systems [27], with a cutoff length scale comparable to the molecular size. In extracting θ_d by the procedure described for θ_0 above, a boundary layer of thickness $\sim 1 r_c$ has been excluded, as within the small fluid wedge close to the CL we observe significant deviations from a strictly spherical shape. Qualitatively, we find this distortion accompanied by excessively strong viscous stress that is suspended by significant slip flow over a distance $\sim 1.5 r_c$ away from the contact line. θ_d is thus to be considered an *apparent* contact angle, and the situation is very similar to the one considered in a global asymptotic analysis of the moving CL problem, using continuum hydrodynamics. There, a relation $\theta_0(Ca)$ may contain various length scales as parameters [24,25]. For instance, in the frequently employed expression

$$\theta_d^3 - \theta_0^3 \cong 9Ca \ln(R/s), \qquad Ca \to 0, \qquad (2)$$

valid to leading order in Ca [24], R is an intermediate macroscopic and s a microscopic length scale, which specifies the length over which slip flow close to the CL occurs.

Figure 4b) displays our numerical results for $\theta_d(Ca)$. If we take $9 \ln(R/s)$ as a compound fit parameter, the simulation results are well described by eq. (2) at a slope of 20.79 ± 0.3 for partial wetting. Varying s between $1 r_c$ and $1.5 r_c$ results in $R \sim 10 r_c$–$15 r_c < b$, consistent with the assumption that R should actually be smaller than the linear size of the total system [25]. Within numerical errors, the slope applies to all wetting conditions for large Ca. For $A_{sl} = -40.0$, however, we find a notable deviation from the linear behaviour for small Ca. It has been pointed out recently [25], that in the case of complete wetting the microscopic length s itself depends on Ca, leading to a modified relation of the form

$$\theta_d^3 \cong 9Ca \ln(\alpha Ca^\beta). \qquad (3)$$

β takes a value dependent on the microscopic mechanism that removes the stress singularity at the CL. It should equal $2/3$ in the presence of thick prewetting layers and long-range van der Waals forces and $1/3$ in any other case. Treating now α and β as two independent fit parameters, we find $\alpha = 17.91 \pm 1.45$ and $\beta = 0.39 \pm 0.04$. Due to the short-range forces used in the DPD scheme a value of $1/3$ is expected and indeed is very close to the fitted numerical value.

Discussion and conclusions. – In summary, we have presented a new approach to model adhesive, solid boundaries in the framework of many-body DPD. The solid phase is represented as a "quenched" liquid and can maintain a specified solid structure. As a certain thermal roughness is retained, a slightly diffuse *sl*-interface results which naturally avoids artefacts such as particle layering or temperature oscillations, and establishes a smooth density profile. Despite its diffuse nature, a wetting-dependent location of a *sl*-interface can be identified, showing weak slip flow with increasing hydrophobicity of the wall. The behaviour of static contact angles is in accord with Young's law if all interfacial and surface tensions are determined independently. The behaviour of dynamic contact angles under constant forced wetting is not only consistent with Cox's hydrodynamic model [24], but also resolves fine details of the relation $\theta_{\mathrm{d}}(\mathsf{Ca})$ that are to be expected for $\mathsf{Ca} \to 0$ in case of complete wetting. To our knowledge, this is the first time that this could be observed in a particle-based simulation scheme.

We emphasize that except wettability, none of the properties of the *sl*-system created has been imposed. They rather follow from the attempt to establish a seamless transition of MDPD forces at the interface. This is in marked contrast to other approaches where additional mechanisms (*e.g.* particle reflection [14], averaging procedures [13]) are employed to achieve a *predefined* boundary condition (*e.g. no slip*). That the *sl*-interface of this work performs quite well with respect to representing standard phenomena of static and dynamic wetting is interesting and encouraging, as the force law used here is still rather generic in character. It might in fact consciously be used to represent more specific solid-liquid systems in an explorative manner. To this end, the current model describes wetting of simple fluids at smooth, low-energy surfaces, and readily extends to chemically patterned (*i.e.* the wetting conditions, by varying A_{sl} spatially) or geometrically textured ones. Thus, the simulation of wetting/dewetting dynamics on micro-textured substrates should be an immediate and important field of application of the presented wall model.

$* * *$

REFERENCES

[1]   Herminghaus S. *et al.*, *J. Phys.: Condens. Matter*, **12** (2000) A57.
[2]   Hirt C. W. and Nichols B. D., *J. Comput. Phys.*, **39** (1981) 201.
[3]   de Gennes P. G., *Rev. Mod. Phys.*, **57** (1985) 827.
[4]   Sbragaglia M. *et al.*, *Phys. Rev. E*, **75** (2007) 026702.
[5]   Hoogerbrugge P. J. and Koelman J. M. V. A., *Europhys. Lett.*, **19** (1992) 155.
[6]   Espanol P. and Warren P. B., *Europhys. Lett.*, **30** (1995) 191.
[7]   Groot R. D. and Warren P. B., *J. Chem. Phys.*, **107** (1997) 4423.
[8]   Latva-Kokko M. and Rothman D. H., *Phys. Rev. Lett.*, **98** (2007) 254503.
[9]   Warren P. B., *Phys. Rev. E*, **68** (2003) 066702.
[10] Pagonabarraga I. and Frenkel D., *J. Chem. Phys.*, **115** (2001) 5015.
[11] Merabia S. and Pagonabarraga I., *Eur. Phys. J. E*, **20** (2006) 209.
[12] Tiwari A. and Abraham J., *Phys. Rev. E*, **74** (2006) 056701.
[13] Pivkin I. V. and Karniadakis G. E., *Phys. Rev. Lett.*, **96** (2006) 206001.
[14] Revenga M., Zuniga I. and Espanol P., *Comput. Phys. Commun.*, **122** (1999) 309.
[15] Pivkin I. V. and Karniadakis G. E., *J. Comput. Phys.*, **207** (2005) 114.
[16] Revenga M., Zuniga I., Espanol P. and Pagonabarraga I., *Int. J. Mod. Phys. C*, **9** (1998) 1319.
[17] Visser D. C., Hoefsloot H. C. and Iedema P. D., *J. Comput. Phys.*, **205** (2005) 626.
[18] Kong B. and Yang X., *Langmuir*, **22** (2006) 2065.
[19] Allen M. P. and Tildesley D. J., *Computer Simulation of Liquids* (Oxford University Press, Oxford) 1987.
[20] Trofimov S. Y., Nies E. L. F. and Michels M. A. J., *J. Chem. Phys.*, **117** (2002) 9383.
[21] Baker J. A. *et al.*, *J. Chem. Phys.*, **122** (2005) 154503.
[22] Thompson P. A. and Robbins M. O., *Phys. Rev. A*, **41** (1990) 6830.
[23] Nijmeijer M. J. P., Bruin C. and Bakker A. F., *Phys. Rev. A*, **42** (1990) 6025.
[24] Cox R. G., *J. Fluid Mech.*, **168** (1986) 169.
[25] Eggers J. and Stone H. A., *J. Fluid Mech.*, **505** (2004) 309.
[26] Dussan V. E. B., *Annu. Rev. Fluid Mech.*, **11** (1979) 371.
[27] Thompson P. A. and Robbins M. O., *Phys. Rev. Lett.*, **63** (1989) 766.